Development of an 11-channel multi wavelength imaging diagnostic for divertor plasmas in MAST Upgrade

ⓘ X. Feng, A. Calcines, ⓘ R. M. Sharples, et al.

COLLECTIONS

Paper published as part of the special topic on Proceedings of the 23rd Topical Conference on High-Temperature Plasma Diagnostics

View Online   **Export Citation**   **CrossMark**

ARTICLES YOU MAY BE INTERESTED IN

Design and implementation of a portable diagnostic system for Thomson scattering and optical emission spectroscopy measurements
Review of Scientific Instruments **92**, 063002 (2021); https://doi.org/10.1063/5.0043818

2D measurements of plasma electron density using coherence imaging with a pixelated phase mask
Review of Scientific Instruments **92**, 073506 (2021); https://doi.org/10.1063/5.0050704

Multi-energy reconstructions, central electron temperature measurements, and early detection of the birth and growth of runaway electrons using a versatile soft x-ray pinhole camera at MST
Review of Scientific Instruments **92**, 073502 (2021); https://doi.org/10.1063/5.0043672

Development of an 11-channel multi wavelength imaging diagnostic for divertor plasmas in MAST Upgrade

View Online   Export Citation   CrossMark

X. Feng,[1,a)] A. Calcines,[1] R. M. Sharples,[1] B. Lipschultz,[2] A. Perek,[3] W. A. J. Vijvers,[3,b)] J. R. Harrison,[4] J. S. Allcock,[4] Y. Andrebe,[5] B. P. Duval,[5] R. T. Mumgaard,[6,c)] MAST-U Team, and EUROfusion MST1 Team[d)]

AFFILIATIONS

[1] Centre for Advanced Instrumentation, Durham University, South Road, Durham DH1 3LE, United Kingdom
[2] York Plasma Institute, University of York, York YO10 5DQ, United Kingdom
[3] Dutch Institute for Fundamental Energy Research (DIFFER), De Zaale 20, 5612 AJ Eindhoven, The Netherlands
[4] CCFE, Culham Science Centre, Abingdon, Oxon OX14 3DB, United Kingdom
[5] Ecole Polytechnique Fédérale de Lausanne (EPFL), Swiss Plasma Center (SPC), 1015 Lausanne, Switzerland
[6] Plasma Science and Fusion Center MIT, Cambridge, Massachusetts 02139, USA

Note: Paper published as part of the Special Topic on Proceedings of the 23rd Topical Conference on High-Temperature Plasma Diagnostics.
a)**Author to whom correspondence should be addressed:** xiande.feng@durham.ac.uk
b)**Current address:** Chromodynamics BV, 5656 AE Eindhoven, The Netherlands.
c)**Current address:** Commonwealth Fusion Systems, Cambridge, MA 02139, USA.
d)See the EUROfusion MST1 Team list of B. Labit *et al.*, Nucl. Fusion **59**, 086020 (2019).

ABSTRACT

Divertor detachment and alternative divertor magnetic geometries are predicted to be promising approaches to handle the power exhaust of future fusion devices. In order to understand the detachment process caused by volumetric losses in alternative divertor magnetic geometries, a Multi-Wavelength Imaging (MWI) diagnostic has recently been designed and built for the Mega Amp Spherical Tokamak Upgrade. The MWI diagnostic will simultaneously capture 11 spectrally filtered images of the visible light emitted from divertor plasmas and provide crucial knowledge for the interpretation of observations and modeling efforts. This paper presents the optical design, mechanical design, hardware, and test results of an 11-channel MWI system with a field of view of 40°. The optical design shows better than 5 mm FWHM spatial resolution at the plasma on all 11 channels across the whole field of view. The spread of angle of incidence on the surface of each filter is also analyzed to inform the bandwidth specification of the interference filters. The results of the initial laboratory tests demonstrate that a spatial resolution of better than 5 mm FWHM is achieved for all 11 channels, meeting the specifications required for accurate tomography.

I. INTRODUCTION

Heat exhaust physics in the divertor is one of the main challenges in realizing magnetic confinement fusion. Divertor detachment, which involves a variety of atomic and molecular processes and can lead to reduced heat and particle fluxes on the divertor, is predicted to be crucial for handling the heat exhaust issue,[1,2] and it is well known that alternative divertor magnetic topology could

further facilitate the reduced heat load.[3,4] MAST Upgrade (MAST-U) will have unprecedented flexibility to tailor the magnetic geometry to improve the understanding of detachment onset and control in conventional and alternative divertor configurations.[5] In order to understand the dynamics of the detachment process and the physics of detachment in the MAST-U divertor, a Multi-Wavelength Imaging (MWI) diagnostic has recently been built to diagnose the emission front and infer recombination rates from Balmer line

intensities.[6,7] The MWI will also measure 2D distributions of electron density and electron temperature in divertor plasmas through line intensity ratios of deuterium Balmer lines[8] and helium singlet and triplet lines.[9–11] The inferred 2D map of plasma parameters, combined with localized measurements from Langmuir probes/Thomson scattering systems and 1D emission-weighted plasma profiles from spectroscopy, will provide crucial knowledge for the interpretation of observations. MWI data will also be used as input to integrated data analysis[12] and for constraining divertor plasma simulations. The MWI is a diagnostic that uses a polychromatic configuration with narrow bandwidth interference filters and CMOS cameras to simultaneously capture 11 spectrally filtered images (380–750 nm) of divertor plasmas. The design has been developed based on a previous four-channel Multi-Spectral Imaging system (MSI)[13] and a ten-channel Multispectral Advanced Narrowband Tokamak Imaging System (MANTIS)[14,15] on the Tokamak à Configuration Variable (TCV) tokamak. The design of the MWI was extended to 11 channels to allow the future incorporation of a coherence imaging channel for measurements of plasma flows[16] and Stark broadening.[17] Comparing with previous multiple spectral imaging diagnostics that use beam splitter or dichroic mirror approaches, the polychromatic layout is better able to support large numbers of filtered image views and emission lines closely spaced in wavelength. This paper focuses on the systematic analysis of the optical design, mechanical design with integration of the *in situ* calibration method, and quantification of the image quality of the multi-wavelength imaging instrument, which are not discussed before in the similar systems.

II. OPTICAL PERFORMANCE OF THE MWI SYSTEM

In order to view the whole divertor on MAST-U, the MWI optics have a field of view of 40° and are composed of separate relay optics and polychromatic optics. Figure 1(a) shows a Zemax ray tracing of the MWI optical design including the schematic drawing of the calibration arm. The relay optics are composed of six 50 mm aperture off-the-shelf commercial lenses (L1–L6 in Fig. 1) and two 100 mm aperture plano convex lenses (L7 and L8 in Fig. 1) with anti-reflection coating to reduce the intensity loss. L1 and L2 are achromatic doublet lenses with a focal length of 75 mm (Thorlabs AC508-075-A), L3 is a positive meniscus lens with 300 mm focal length (Thorlabs LE1985-A), L4 is an achromatic doublet lens with a focal length of 500 mm (Thorlabs AC508-500-A), L5 and L6 are achromatic doublet lenses with a focal length of 750 mm (Thorlabs AC508-750-A), and L7 and L8 have a focal length of 800 mm (OptoSigma SLB100-800PM). Figure 1(b) shows the zoomed-in view of L1–L6 in the relay optics, and Fig. 1(c) shows the zoomed-in view of the optics L1–L3 that have the same arrangement as the optics L1–L3 in the original arm and a mirror that will be manually inserted into a 60 mm cage to switch to the *in situ* calibration. The relay optics generate an intermediate image of the object field at a position ~20 mm after the last lens in the relay optics (L8). This intermediate image can be used for *in situ* focus adjustment and image quality assessment for all the cameras. The polychromator, which has the same configuration as MANTIS,[14,15] is, in turn, based on the original polychromator design for the motional-Stark effect diagnostic on Alcator C-MOD.[18] Each polychromator in the MWI is composed of a field lens with a focal length of 750 mm (achromatic
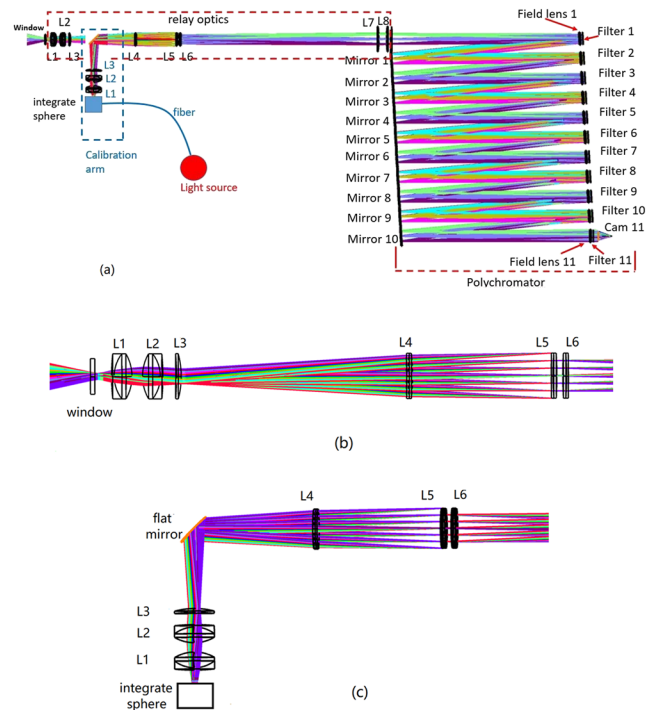

FIG. 1. (a) Zemax ray tracing of the MWI optical design including the schematic drawing of the calibration arm. Only one camera is shown (on channel 11). (b) Zoomed-in view of L1–L6 in the original relay optics. (c) Zoomed-in view of the optics (L1–L3 and flat mirror) in the calibration arm.

doublet lens), a bandpass interference filter, a dielectric coating concave mirror with a curvature radius of 768 mm, camera lens, and a CMOS camera. The polychromator is operating off-axis with a cavity angle of $\theta = 3°$ following a trade-off study between image quality and space required for the field lens, filter holder, and camera. The focal length of the field lens is chosen to be the same as the distance from the intermediate image position to the field lens so the beam after the field lens becomes collimated. The filter located after the field lens transmits the wavelength of interest and reflects the rest of the spectral range to the field lens again to produce an intermediate image on a concave mirror with a focal length of half of that of the field lens. The field mirror acts as a 1:1 pupil reimaging system for the next channel. This process is repeated over the cavity until the last channel is reached.

For the optical performance of the MWI optics, it is desired that the image quality over the whole field view should be less than 5 mm FWHM to enable high quality tomographic analysis. However, as the MWI has a very large field of view, this is challenging for the optical design. The optical performance has therefore been analyzed extensively in Zemax. Figure 2 shows the focus position (the distance from the camera lens to sensor) and image quality (spatial resolution at the plasma) as a function of channel number. The cameras lens used in the Zemax analysis is a paraxial lens instead of the real camera lens for which the Zemax prescription was not available. The focus position is a function of wavelength and channel, as shown in the top panel in Fig. 2, which shows that the position of the focus
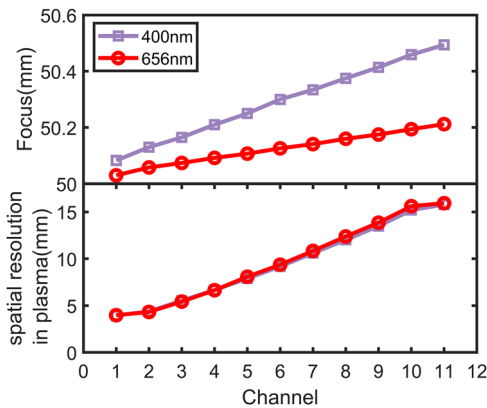
FIG. 2. Focus position of the camera lens and image quality with MWI channel numbers.

FIG. 3. Spatial resolution at the plasma with field of view on different channel numbers and at different focal ratios.

increases with channel numbers for the same wavelength and that within the same channel, the focus position varies with wavelength. This means that focus adjustment is required when changing the filter and an *in situ* focus calibration method is needed (see below). The bottom panel in Fig. 2 shows that the image quality deteriorates with the channel number as expected due to the effect of additional optics for both wavelengths, and the image quality after the third channel does not meet our requirement. For this analysis, the paraxial lens in front of the detector has the same aperture stop setting for all the channels and is equal to the maximum lens aperture. The image quality plotted here is an average of 11 points in the field of view with one point on the axis and two orthogonal points on the 5°, 10°, 20°, 30°, and 40° field of view circle. Further analysis shows which aberrations (e.g., spherical aberration) in the system are accumulating with the channel number leading to the deterioration of image quality. The polychromator has the capability to self-cancel certain off-axis aberrations, such as coma, which depend on the angle of field of view due to the flip of the image by the concave mirror on consecutive channels, as described in detail in Ref. 18. However, the spherical aberration, which dominates other aberrations due to the wide field of view of the system, is accumulated, and the best way to minimize such aberrations is to reduce the numerical aperture by stopping down the camera lens.

Figure 3 shows the spatial resolution of the MWI system as a function of channel number and field of view from the Zemax model. The solid lines show the results at the maximum paraxial lens aperture of f/1.4. It can be seen that the spatial resolution from channel 4 onward at full aperture will be larger than our requirement but that stopping down the lens to f/2.8 could improve the image quality to make it less than 5 mm FWHM over the whole field of view. From channel 7 onward, further stopping down of the paraxial lens to f/4.2 is needed to maintain the image quality. Although stopping down the camera lens will lead to reduced throughput to the sensor, this strategy can work for the MWI system since the brightness of different lines (wavelengths) varies significantly in divertor plasmas. For example, the Dα line can be 1000 times brighter than Dε in a typical divertor plasma, and so the Dα filter could be put into one of the latter channels to achieve good spatial resolution with still enough signal on the camera sensor. This strategy has been verified with the
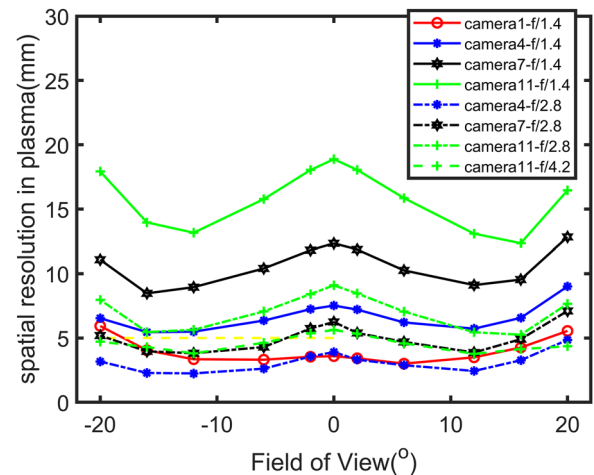
MANTIS system.[15] Finalizing the camera lens f/# number is therefore a trade-off between the throughput and image quality and is currently the subject of a study to find the best permutation of filters in the system.

In the MWI optics, the bandpass interference filter that works as a beam splitter is a key optical component. Inappropriate selection of the bandwidth of the filter can cause vignetting across the field of view due to the well-known shift of the filter bandpass with incident angle. The influence of the reflective surface in the filter on the image quality in the imaging system is also important and is discussed in detail elsewhere.[15] Here, we present a simulation of the 2D distribution of angle of incidence (AOI) on the filter surface to inform the filter bandwidth specification. Figure 4 shows the 2D map of the AOI on the odd channel filter surface. The AOI ranges from 0.5° to 5.5° on all the filters, while the AOI map on the even channel is flipped relative to that on an odd channel due to the reflection by the mirrors in the polychromator.
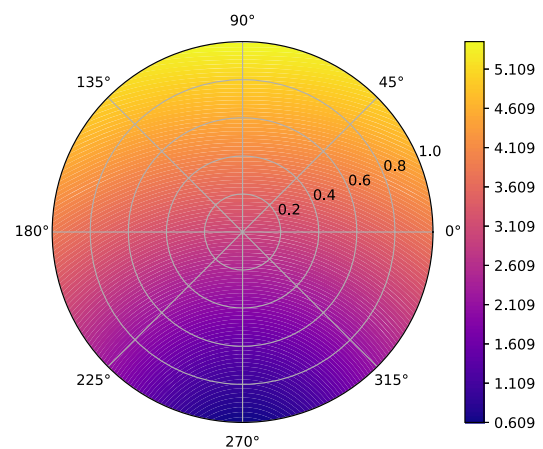

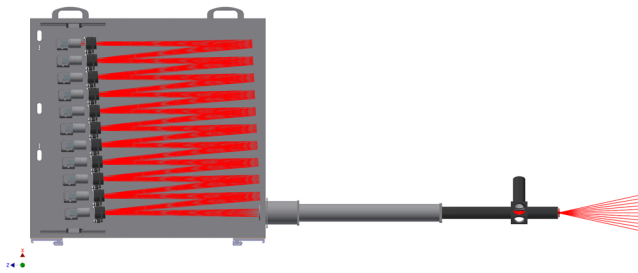**FIG. 4.** 2D distribution of angle of incidence (degrees) on the filter surface in odd channels.

FIG. 5. Mechanical design of the MWI system showing the calibration arm. A fold mirror is manually inserted when the calibration arm is in use.

III. MECHANICAL DESIGN OF THE MWI SYSTEM

The mechanical parts of the MWI system are designed based on the Zemax optical model. A CAD model of the optical layout generated from Zemax was integrated into the mechanical design to ensure that the optics fitted properly into the mechanical parts. The field lens is placed in a commercial kinematic mount in combination with the filter. The camera is mounted to a five-axis stage in combination with the camera lens. Both mounts have the capability to fine adjust the tilt angle and are attached to a common plate that is installed on a rail guide system, allowing the adjustment of the cavity length by ±50 mm. As discussed in Sec. II, *in situ* focus adjustment is needed if the filter order is changed. Therefore, a calibration arm with a 2-in. diameter integration sphere is implemented and a circular crosshair contact reticle will be installed in the intermediate image plane to achieve the *in situ* calibration. The calibration arm is placed between lens 3 and lens 4 in the relay optics (see Fig. 1), but orthogonal to the original arm, and having the same lens 1–3 optics as the original arm. Access to the calibration arm light path is via a manually inserted fold mirror (Fig. 5).

IV. HARDWARE

Most of the optical lenses and mounts used in the MWI system, except for the mirrors and filters, are off-the-shelf products to reduce the time and cost for implementation. As the concave mirrors are located at the position of the intermediate image plane, high specification mirrors with irregularity of ≤1/4 lambda, scratch-dig number of 40/20, and a high reflectivity (>99%) dielectric coating in the spectral range 380–750 nm are used. The bandpass interference filters with high transmission (>90%) in the passband and high reflection (>99.9%) outside the passband are selected to maintain the high throughput and avoid ghost images. Besides the optical components, the synchronization of the cameras and the data acquisition system are of vital importance for the multi-camera diagnostic. For the MWI, we choose 11 XIMEA PCIe CMOS cameras with Sony IMX252 sensors. A 12-port switch controls and aggregates all the camera data and transfers the data at up to 8 GB/s over a single fiber cable to an acquisition computer. The cameras, data acquisition system, and the hardware interface code used in the MWI are the same as those of the MANTIS system, which has been tested on the TCV tokamak.[15]

V. SYSTEM PERFORMANCE

For imaging systems, the Modulation Transfer Function (MTF) is a fundamental tool for assessing performance. There are three kinds of targets that may be used to measure the MTF:[19] slanted-edge target, sine-wave target, and grill pattern. Here, the MTF of the MWI images is measured using the slanted-edge method in which multiple slanted-edge targets are placed in the object plane, and the horizontal and vertical MTF in five different fields of view (one on the axis and the rest distributed azimuthally on a ~20° field of view circle) have been measured using the sfrmat3 method.[20] Figure 6 shows the vertical and horizontal MTF of cameras 1 and 4 with different apertures in the MWI system at the five different field positions. It can be seen in the leftmost figure that the average spatial frequency where the MTF reaches a value of 0.5 for camera 1 with f/1.4 (maximum aperture) is ~35 lp/mm, corresponding to a spatial resolution in the object plane of 330/(2 × 35) mm = 4.7 mm, where 330 is the demagnification factor of the optics and the factor 2 corrects for the two lines in a pair. There is a slight difference between the vertical and horizontal MTF at each position, which is possibly caused by the astigmatism aberration due to the off-axis system. The middle panel in Fig. 6 shows that the measured horizontal MTF of camera 4 at f/1.4 is better than the vertical MTF and even better than the horizontal MTF of camera 1, but the vertical MTF of camera 4 is worse than that of camera 1. This is because the focus for camera 4 was optimized for the horizontal direction and not for the vertical direction, which could be corrected by adjusting the focus plane. The average spatial frequency of camera 4 is similar to that of camera 1. By stopping down the camera lens to f/2.8 in camera 4, the average spatial frequency at an MTF value of 0.5 increases due to the improving image quality. Figure 7 shows the improvement of the overall image quality from stopping down the lens on camera 10. The average spatial frequency at the MTF value of 0.5 is ~20 lp/mm at f/1.4, corresponding to 8.25 mm spatial resolution in the object plane. Stopping down the camera lens to f/4.0 would improve the overall spatial resolution to ~4.5 mm. Although the measured image quality of the MWI system is not exactly the same as that in the simulation in Fig. 3, the overall trend of the measured image quality
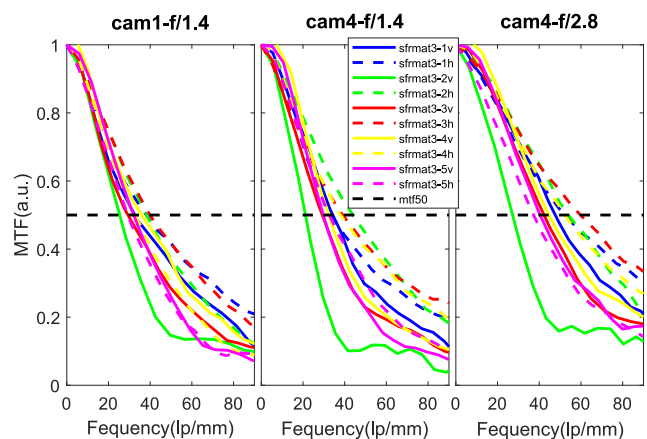

FIG. 6. Measured vertical and horizontal MTFs of cameras 1 and 4 at five different fields of view with different apertures in the MWI system.
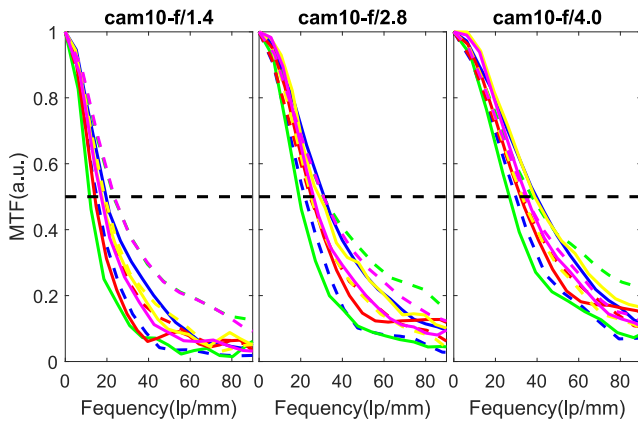
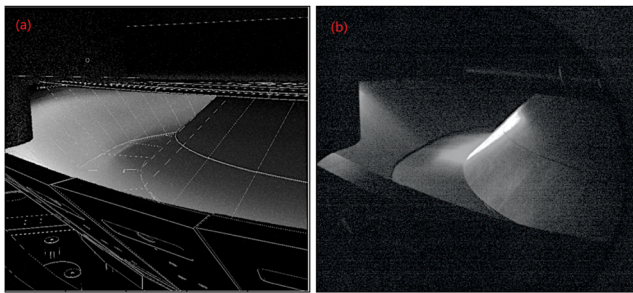**FIG. 7.** Measured vertical and horizontal MTFs of camera 10.

FIG. 8. (a) Modeled divertor plasma view by CHERAB. (b) Actual divertor view illuminated by a flash lamp.

VI. SUMMARY

An 11-channel multi-wavelength imaging system has been developed for MAST-U to diagnose 2D plasma parameters in the super-X divertor and explore the influence of magnetic topology on detachment physics. The optical design and mechanical design are described in detail. Optical system performance measurements show that less than 5 mm FWHM spatial resolution at the plasma can be achieved over the whole field of view. Comparing with previous multi-wavelength imaging systems, the polychromator layout in the MWI reserves the space for integration of other imaging diagnostics, such as coherence imaging spectroscopy to measure 2D impurity flows[16] and electron density maps[17] in the plasma to expand the capabilities of the MWI system.

DATA AVAILABILITY

The data that support the findings of this study are available from the corresponding author upon reasonable request.

with the channel number and camera lens f/# number matches well with the simulation result. The discrepancies between the simulation and measured image quality could be caused by multiple factors, including the non-ideal (non-paraxial) nature of the off-the-shelf camera lens and any residual alignment errors. Figure 8(b) shows the actual divertor view illuminated by a flash lamp. For comparison, the modeled divertor plasma view by CHERAB[21] is shown in Fig. 8(a).

Preliminary relative intensity calibration of the MWI system using a 2-in. diameter un-calibrated integrating sphere shows that each channel has a flat response within ±5%. Further absolute calibration of the MWI system is ongoing to specify the calibration factors for each pixel in the field of view. Ideally, the full MWI system would be calibrated with an integrating sphere after installation on MAST-U; however, this is not practical for the MWI system as there is no space near the port to put the absolute calibrated integrate sphere close to the system. Therefore, absolute calibration will be made in the laboratory with a calibrated integrate sphere, and *in situ* relative intensity calibration with the 2-in. integrating sphere will be employed after installation on MAST-U to regularly check the calibration factor for each pixel.

REFERENCES

[1] R. A. Pitts *et al.*, J. Nucl. Mater. **438**, S48–S56 (2013).
[2] A. Loarte *et al.*, Nucl. Fusion **47**, S203–S263 (2007).
[3] B. Lipschultz *et al.*, Nucl. Fusion **56**, 056007 (2016).
[4] D. Moulton *et al.*, Plasma Phys. Controlled Fusion **59**, 065011 (2017).
[5] J. R. Harrison *et al.*, Nucl. Fusion **59**, 112011 (2019).
[6] D. Lumma *et al.*, Phys. Plasmas **4**, 2555 (1997).
[7] J. L. Terry *et al.*, Phys. Plasmas **5**, 1759 (1998).
[8] J. Karhunen *et al.*, Nucl. Mater. Energy **25**, 100831 (2020).
[9] M. Griener *et al.*, Plasma Phys. Controlled Fusion **60**, 025008 (2017).
[10] S. Lisgo *et al.*, J. Nucl. Mater. **390-391**, 1078 (2009).
[11] O. Schmitz *et al.*, Plasma Phys. Controlled Fusion **50**, 115004 (2008).
[12] C. Bowman *et al.*, Plasma Phys. Controlled Fusion **62**, 045014 (2020).
[13] B. L. Linehan *et al.*, Rev. Sci. Instrum. **89**, 103503 (2018).
[14] W. A. J. Vijvers *et al.*, J. Instrum. **12**, C12058 (2017).
[15] A. Perek *et al.*, Rev. Sci. Instrum. **90**, 123514 (2019).
[16] S. A. Silburn *et al.*, Rev. Sci. Instrum. **85**, 11D703 (2014).
[17] J. S. Allcock, "New techniques for coherence imaging of fusion plasmas," Ph.D. dissertation, Durham University, 2020.
[18] R. T. Mumgaard, "Engineering upgrades to the motional Stark effect diagnostic on Alcator C-mod," M.S. thesis, Massachusetts Institute of Technology, Cambridge, 2015.
[19] X. Zhang *et al.*, Proc. SPIE **8293**, 829307 (2012).
[20] P. D. Burns and D. Williams, "Camera resolution and distortion: Advanced edge fitting," Electron. Imaging **2018** 171-1–171-5 (2018).
[21] C. Giroud *et al.*, (2018). "CHERAB spectroscopy modelling framework," Zenodo, Version v0.1.0, https://doi.org/10.5281/zenodo.1206142.